

Patch-based Lung Ventilation Estimation using Multi-layer Supervoxels

Adam Szmul^a, Tahreema Matin^b, Fergus V. Gleeson^{b,c}, Julia A. Schnabel^{a,d}, Vicente Grau^a, Bartłomiej W. Papież^{a,e}

^a*Institute of Biomedical Engineering, Department of Engineering Science, University of Oxford, UK,*

^b*Department of Oncology, University of Oxford, UK*

^c*Department of Radiology, Oxford University Hospitals NHS FT, Oxford, UK*

^d*Department of Biomedical Engineering, School of Biomedical Engineering and Imaging Sciences, King's College London, UK*

^e*Big Data Institute, Li Ka Shing Centre for Health Information and Discovery, University of Oxford, UK*

Abstract

Patch-based approaches have received substantial attention over the recent years in medical imaging. One of their potential applications may be to provide more anatomically consistent ventilation maps estimated on dynamic lung CT. An assessment of regional lung function may act as a guide for radiotherapy, ensuring a more accurate treatment plan. This in turn, could spare well-functioning parts of the lungs. We present a novel method for lung ventilation estimation from dynamic lung CT imaging, combining a supervoxel-based image representation with deformations estimated during deformable image registration, performed between peak breathing phases. For this we propose a method that tracks changes of the intensity of previously extracted supervoxels. For the evaluation of the method we calculate correlation of the estimated ventilation maps with static ventilation images

Email address: adam.szmul@eng.ox.ac.uk (Adam Szmul)

acquired from hyperpolarized Xenon129 MRI. We also investigate the influence of different image registration methods used to estimate deformations between the peak breathing phases in the dynamic CT imaging. We show that our method performs favorably to other ventilation estimation methods commonly used in the field, independently of the image registration method applied to dynamic CT. Due to the patch-based approach of our method, it may be physiologically more consistent with lung anatomy than previous methods relying on voxel-wise relationships. In our method the ventilation is estimated for supervoxels, which tend to group spatially close voxels with similar intensity values. The proposed method was evaluated on a dataset consisting of three lung cancer patients undergoing radiotherapy treatment, and this resulted in a correlation of 0.485 with XeMRI ventilation images, compared with 0.393 for the intensity-based approach, 0.231 for the Jacobian-based method and 0.386 for the Hounsfield units averaging method, on average. Within the limitation of the small number of cases analyzed, results suggest that the presented technique may be advantageous for CT-based ventilation estimation. The results showing higher values of correlation of the proposed method demonstrate the potential of our method to more accurately mimic the lung physiology.

Keywords: lung ventilation estimation, supervoxels, XeMRI ventilation, deformable registration

1. Introduction

Patch-based methods have become an essential tool in many fields of computer vision and medical imaging. In computer vision they are used for

4 object localization and class segmentation [1], human pose [2] and depth
5 estimation [3, 4], or to generate image descriptors [5, 6, 7]. There has also
6 been a surge of growth of their application in medical imaging. They have
7 been successfully applied to enhance image segmentation [8, 9], as well as
8 to tumor segmentation [10, 11, 12] or analysis of its texture [13]. For lung
9 image analysis, they have been applied, for instance, to enhance resolution
10 of 4D computed tomography (4DCT) [14]. Other applications are patch-
11 based descriptors for image similarity measure [15, 16] and patch-based image
12 registration approaches [17, 18, 19].

13 A potential application of patch-based methods is to estimate regional
14 ventilation of the lungs based on 4DCT. This is an important application, as
15 pulmonary-related diseases are among the leading causes of death worldwide
16 [20]. Lung cancer is the most common cause of cancer death and the second
17 most commonly diagnosed cancer type in both male and female populations
18 [21], and Chronic Obstructive Pulmonary Disease (COPD) is responsible for
19 nearly twice as many deaths as breast cancer [20]. Tests measuring overall
20 lung condition may not be specific enough to help localize and confront these
21 challenging diseases [22]. The gold standard test for pulmonary function is
22 the spirometry technique, which evaluates global lung function by measuring
23 the volume and speed of air during inhalation and exhalation. Although
24 this method is cheap, fast, and widely used as a screening tool [23], it lacks
25 regional lung evaluation and thus cannot be used for precision medicine such
26 as individualized radiotherapy planning [24]. Assessment of the regional
27 lung functionality has the potential to provide more accurate radiotherapy
28 treatment [25], which could spare well-functioning parts of the lungs and be

29 used for follow up to evaluate the treatment effectiveness.

30 The estimation of ventilation surrogates based on CT images is an active
31 field of research. In [26], for instance the Dice overlap of percentage ven-
32 tilation volumes between 4DCT originating ventilation estimates and ^3He
33 MRI was investigated, and no significant difference was found. That study
34 supports the claim that well-ventilated regions in 4DCT-based ventilation
35 surrogates and ^3He MRI are in agreement. A lobar oriented analysis of lung
36 ventilation was presented in [27], where the authors compared CT-based ven-
37 tilation surrogates with ^3He MRI for asthma patients. The authors found
38 agreement between the investigated ventilation imaging methods. An inter-
39 esting study was presented in [28], where, apart from investigating the corre-
40 lation between different CT-based ventilation estimation techniques and hy-
41 perpolarized gas MRI ventilation images, the correlation between ^3He MRI
42 and ^{129}Xe MRI was evaluated. They found significantly lower correlation
43 between CT originating ventilation surrogates and hyperpolarized gas MRI
44 ventilation maps than between ^3He MRI and ^{129}Xe MRI. In order to search
45 for the best indicator of lung function, the authors of [29] investigated corre-
46 lation between ventilation estimated from ^{129}Xe MRI and the quantity of gas
47 transferred to red blood cells (RBCs). Their initial conclusion was that ^{129}Xe
48 MRI ventilation may not be the optimal measure of the true regional lung
49 function. Despite the amount of work done in the field, there is still scope
50 for further research in the methods dedicated for estimating ventilation from
51 CT images.

52 1.1. Aims

53 The aim of this work is to introduce a patch-based ventilation estima-
54 tion method and perform its evaluation, comparing its results with magnetic
55 resonance imaging with hyperpolarized ^{129}Xe as an inhalable contrast agent
56 (XeMRI). We run a number of experiments to investigate the parameter set-
57 ting and robustness of the method. The original idea and preliminary results
58 were presented in [30]. This paper has been extended in the following way:

- 59 1. We present, in detail, the proposed method for regional ventilation es-
60 timation, including a thorough investigation of the influence of relevant
61 parameters.
- 62 2. We show the performance of our approach for different image registra-
63 tion methods.
- 64 3. We provide a quantitative comparison between state-of-the-art meth-
65 ods for lung ventilation estimation and the proposed method.
- 66 4. We correlate our results with XeMRI using the developed registration
67 approach between proton density MRI (pMRI) and CT, which we ex-
68 plain in detail.

69 The remaining part of this section is organized as follows: in Sec. 1.2
70 we present lung ventilation imaging methods based on MRI and CT. Subse-
71 quently, in Sec. 1.3 we discuss lung image registration when applied to lung
72 CT. We follow this by introducing lung ventilation estimation techniques
73 based on 4DCT in Sec. 1.4.

74 1.2. Lung Ventilation Imaging

75 Lung ventilation imaging allows insight into local lung function. Most of
76 the lung ventilation imaging techniques require the use of ionizing imaging
77 methods and radioactive tracers, such as Single Photon Emission Computed
78 Tomography (SPECT) [31] or Positron Emission Tomography (PET) [32].
79 A lung function imaging technique that has received substantial attention in
80 the field is hyperpolarized noble gas MRI [33, 34]. Its non-ionizing nature
81 makes it a promising technique for imaging ventilation, perfusion and gas
82 transfer within the lungs [34]. In the static approach of this method, the
83 patient breathes in a fixed volume of hyperpolarized noble gas and images
84 are acquired during breath hold. Static hyperpolarized XeMRI provides im-
85 ages with direct visualization of the distribution of the inhaled gas in the
86 patient’s lungs. Compared with the aforementioned lung functional imaging
87 techniques, XeMRI is acquired during a single breath-hold. To allow for the
88 localization of ventilation images with respect to the patient anatomy, pMRI
89 is acquired immediately before XeMRI acquisition. As an extension to the
90 static XeMRI lung ventilation imaging, dynamic XeMRI has been recently
91 proposed [35]. In this method several volumetric images are acquired over a
92 number of breathing cycles in a single imaging. Currently, the main draw-
93 back of the technique is its accessibility, which is limited to a number of
94 imaging centers in the world.

95 4DCT, on the other hand, is a structural imaging technique routinely used
96 for radiotherapy planning, where images are acquired during free breathing
97 under spirometry control. It can be used to estimate lung ventilation maps,
98 based on the results of the registration between peak-exhale and peak-inhale

breathing phase volumes. 4DCT based ventilation methods can be roughly classified into those, which rely on the value of the determinant of the Jacobian matrix of the deformations to estimate the lung volume change [36, 37], methods tracking the changes in the intensity of the lungs quantified in Hounsfield units (HU) [38, 24], and those based on averaging a product of air and tissue fraction across all breathing phases [39]. Changes in tissue attenuation correspond to variations in tissue density and originate from filling the lungs with air. The Jacobian-based and intensity tracking methods require estimation of the deformation field between peak breathing phases from 4DCT, performed by deformable image registration. In contrast, the averaging method [39] does not need to estimate deformations.

1.3. Lung Image Registration

The task of deformable image registration is to bring two or more images into alignment, based on a specified similarity measure. To ensure not only a perfect match for each voxel but also plausibility of the estimated deformation field, a regularization is required. This can be done, for instance, by incorporating it into a transformation model, such as Free Form Deformations (FFDs) with B-Splines [40], by adding an additional regularization term to the optimization [41, 42], or by incorporating sparse key-points matching [43].

To investigate the robustness of the proposed ventilation estimation method on the applied image registration method, we used a number of different approaches: the deeds method [44], classic demons method [45], its extended version applying bilateral filtering (BLF) [41], and supervoxel-based graph cuts [46]. The aim of this experiment is to evaluate if the obtained patterns

124 in the results are independent of the applied image registration method to
125 estimate deformations, rather than to determine which of the methods is the
126 most suitable for this application.

127 In the first method [44] the optimization problem is posed on a minimum
128 spanning tree (MST) extracted from a graph created over a regular grid.
129 Each node in the graph represents a cubic patch of voxels. The authors used
130 a belief propagation as the optimisation technique, which for a MST stated
131 problem can find the global minimum. The final deformation field is achieved
132 by using B-spline interpolation of the resulting sparse optimization outcome.
133 We will refer to this method as: deeds.

134 The second investigated method is the well established demons method
135 [45, 47]. In the primary work [45], the optimization is performed in an
136 alternate way, in which finding the best displacement at each iteration for
137 every voxel is followed by a filtering of the estimated displacement field, where
138 the filtering works as a regularization. The method was later extended to
139 preserve diffeomorphism [47]. The authors used Gaussian filtering, which
140 did not take into account the discontinuities appearing at the borders of
141 the lungs. Such a limitation was shown to result in the underestimation of
142 displacements near the borders of the lungs. We will refer to this method as
143 demons.

144 The third evaluated method is an extension of the previous. In [41], the
145 authors addressed the problem of preservation of discontinuities at the bor-
146 ders of the lungs, called sliding motion, by introducing an additional filtering
147 kernel in the form of bilateral filtering (BLF) [48]. The method showed an
148 improvement in accuracy of the results, as well as more anatomically plau-

149 sible deformations, especially within problematic lung regions. We will refer
150 to this method as demons BLF.

151 The fourth method [46] applies graph cuts [49] as an optimization method
152 over the images previously clustered into supervoxels. In the optimization
153 step for each of the supervoxels the best displacement is found from a pre-
154 defined set of allowed displacements. As a result of this step we obtain a
155 deformation estimated for each of the supervoxels. A direct application of
156 this displacement to all of the voxels belonging to the supervoxel might re-
157 sult in foldings at the borders of supervoxels that have different deformations
158 and thus physiologically implausible deformations. This issue has been ad-
159 dressed by applying guided image filtering [50], akin to [51]. The resulting
160 displacement field remains smooth in the homogeneous regions, at the same
161 time preserving discontinuities at the borders of the organs, such as those
162 between the lungs and rib cage or lungs and diaphragm. In the following
163 part of the paper this method will be referred to as supervoxel graph cuts.

164 All of the methods have shown good performance in a publicly available
165 Dir-Lab dataset [52], with 300 manually annotated landmarks provided for
166 evaluation purpose. The deeds method resulted in Target Registration Er-
167 ror (TRE) on the dataset of 1.43mm, for Demons and their BLF extension
168 TREs of 2.35mm and 1.95mm were measured, respectively, and for the su-
169 pervoxel graph cuts TRE was 1.16mm. All registration methods used for
170 the evaluation of our new method for ventilation estimation were optimized
171 using Dir-Lab, and all of them were optimized by their authors to get the
172 best TRE on Dir-Lab. We have applied them with the provided parameters.
173 These image registration method parameters were set completely indepen-

dent of our testing dataset. There are other lung image registration methods [53, 54] and even approaches dedicated for lung mass/tissue preserving during the alignment process [55, 56, 57]. These methods, though presenting an interesting approach for enhancing similarity measure, resulted in moderate performance when evaluated on the Dir-Lab dataset. Our choice covers main registration categories in terms of optimization, namely: discrete, continuous, and hybrid.

1.4. Ventilation Estimation from 4DCT

There are several methods to estimate ventilation from 4DCT. In this section we discuss the existing approaches for this task, starting from those requiring estimation of the displacement field. These methods can be divided into intensity-based [24, 38] and Jacobian-based [36, 37] methods. We then present the method which applies the relation between air and tissue fraction and does not require image registration [39].

Intensity/Density Change Ventilation Estimation Method: One of the approaches for ventilation estimation from 4DCT is to track changes in lung intensity throughout the breathing process. As CT intensity is directly related to the tissue density, it reflects the changes originating from filling the lungs with air. Following [24, 58], the ventilation is estimated for the full exhale phase:

$$Vent_{Dens}^{exh}(\mathbf{x}) = \left(\frac{HU_{exh}(\mathbf{x}) * G_{k1} - HU_{inh}(\mathbf{x} + \mathbf{u}_{inh}) * G_{k1}}{HU_{inh}(\mathbf{x} + \mathbf{u}_{inh}) * G_{k1} + 1000} \right) * G_{k2}, \quad (1)$$

with $HU_{exh}(\mathbf{x} + \mathbf{u}_{exh})$ being an intensity value expressed in Hounsfield units (HU) for a voxel at spatial position \mathbf{x} of the peak exhale phase image warped

196 towards the peak inhale phase image by the displacement field \mathbf{u}_{inh} . Similarly,
 197 $HU_{inh}(\mathbf{x})$ represents intensity value of peak inhale image for the same voxel \mathbf{x} .
 198 G_{k1}, G_{k2} are Gaussian kernels used for smoothing and convolved (denoted by
 199 $*$ in the equation) with the images. Some researchers substituted Gaussian
 200 kernels with box filter kernels, [59], or with median filter kernels, [28, 60]. In
 201 our study we followed the original formulations of [24, 58], therefore, we will
 202 subsequently refer to the Gaussian filtering. The investigation of the influence
 203 of the applied filtering methods was out of the scope of this work. In [61]
 204 the authors investigated the reproducibility of the intensity-based approach
 205 for a number of different parameters and cases. All the image intensities are
 206 given in HU.

207 *Jacobian-based Method:* Local lung volume change can be used as a mea-
 208 sure of lung ventilation [36]. The determinant of the Jacobian of deformations
 209 estimated by deformable registration between different breathing phases is.

$$Vent_{JAC}(\mathbf{x}) = \begin{vmatrix} 1 + \frac{\partial u_x(\mathbf{x})}{\partial x} & \frac{\partial u_x(\mathbf{x})}{\partial y} & \frac{\partial u_x(\mathbf{x})}{\partial z} \\ \frac{\partial u_y(\mathbf{x})}{\partial x} & 1 + \frac{\partial u_y(\mathbf{x})}{\partial y} & \frac{\partial u_y(\mathbf{x})}{\partial z} \\ \frac{\partial u_z(\mathbf{x})}{\partial x} & \frac{\partial u_z(\mathbf{x})}{\partial y} & 1 + \frac{\partial u_z(\mathbf{x})}{\partial z} \end{vmatrix} \quad (2)$$

210 with u_x, u_y, u_z being the deformation fields estimated in x, y and z directions
 211 respectively. The determinant of the Jacobian of the deformations taking val-
 212 ues between 0 and 1 indicate for shrinking the lung volume, values of 1 mean
 213 no volume change for the region and values over 1 indicate volume expansion
 214 calculated for a spatial location \mathbf{x} . Such an approach has been applied in [37],
 215 where XeCT-based ventilation volumes were compared with the ventilation
 216 estimated based on the determinant of the Jacobian. Recently a sensitiv-
 217 ity analysis of the determinant of the Jacobian for lung cancer treatment

218 planning has been presented [62]. The reproducibility of the Jacobian-based
 219 ventilation has been investigated in [63]. It has been shown that the method
 220 correlates well with lung function in emphysema patients [58].

221 *Air/tissue Fraction Averaging Method:* In contrast to previously pre-
 222 sented methods, the HU-based method [39] does not require image regis-
 223 tration between breathing phases. Instead of performing image registration
 224 between full inhale and full exhale phases, the authors propose to estimate
 225 lung ventilation in terms of a product of air and tissue fractions density
 226 calculated locally for all of the breathing phases and subsequently averaged
 227 across them:

$$Vent_{HU}(\mathbf{x}) = \frac{1}{N} \sum_{\phi=1}^N V_{\phi}(\mathbf{x}) \quad (3)$$

$$V_{\phi}(\mathbf{x}) = \begin{cases} \frac{HU_{\phi}(\mathbf{x})}{-1000} \times \frac{HU_{\phi}(\mathbf{x})+1000}{1000} & \text{for } \mathbf{x} \in L(\phi) \\ 0 & \text{for } \mathbf{x} \notin L(\phi) \end{cases} \quad (4)$$

228 where ϕ is a current number of the breathing phase in 4DCT with N be-
 229 ing the total number of breathing phases, and L is the mask of the lungs
 230 delineated from the peak inhale phase. The method was reported to have
 231 good correlation with Galligas PET for normal patients control group but
 232 it failed to achieve the same accuracy for individuals with severe ventilation
 233 distortions. Such behavior could be expected due to the estimation of the
 234 ventilation based on a relation between air and tissue fraction for a single
 235 phase. A clearly problematic case is the detection and evaluation of the air
 236 trapped in the lungs for patients with severe Chronic Obstructive Pulmonary
 237 Disease (COPD).

238 The remaining part of this paper is organized in the following way: in

239 Sec. 2 we introduce our proposed method for estimating ventilation in a
 240 patch-based manner. The results of the proposed experiments are presented
 241 in Sec. 3, which are finally discussed and concluded in Sec. 4.

242 **2. Methods**

243 In this section we present the proposed supervoxel-based lung ventilation
 244 estimation method. We introduce the image clustering method in Sec. 2.1,
 245 as well as explain how we apply it to the proposed method in Sec. 2.2. A
 246 work-flow diagram presenting the method is shown in Fig. 1. Finally in Sec.
 247 2.3 we present the proposed image registration framework in which we bring
 248 the estimated ventilation maps from 4DCT to align with XeMRI ventilation
 249 images.

250 *2.1. Supervoxel clustering*

251 One of the approaches for patch-based methods is supervoxel-based im-
 252 age representation. Supervoxel-based image clustering groups voxels that are
 253 spatially close and visually similar into larger structures. They have become
 254 the building blocks for many applications in computer vision and medical im-
 255 age analysis. In our formulation, we apply Simple Linear Iterative Clustering
 256 (SLIC) [64] as a clustering method, due to its speed of performance and direct
 257 control over the number of extracted supervoxels and supervoxel compact-
 258 ness. The SLIC method is designed to extract k approximately equally-sized
 259 supervoxels. Initially, seeds of the supervoxels are placed on a regular grid at
 260 intervals $S = \sqrt[3]{M/k}$ voxels apart, with M being the total number of voxels
 261 in the image. In the original work by Achanta [64], the method was proposed
 262 for 2D images, whereas here we apply it to 3D supervoxels. The positions of

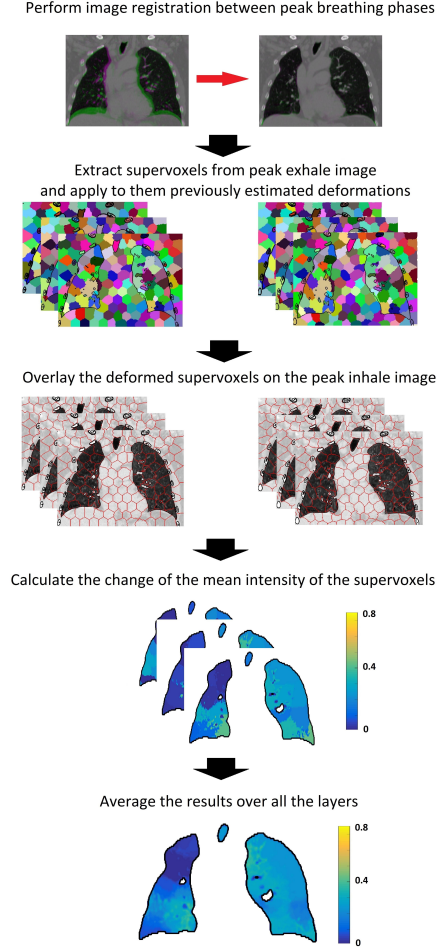


Figure 1: The diagram shows the work-flow of the proposed approach for patch-based lung ventilation estimation. We start by performing deformable image registration between peak breathing phase volumes. We follow that by clustering the peak exhale image into a number of supervoxels. We extract a number of layers of supervoxels, each with slightly different initial parameters, which is depicted in the figure by multiple boxes for the current and following steps. After that we apply the previously estimated deformations to the extracted supervoxels. The original supervoxels extracted from the peak exhale image are interpolated and labeled using the same color. For the initial position of the supervoxels their mean intensity values are calculated. We map the warped supervoxels over the peak inhale image to calculate changes in their mean intensity between the mapping over the peak exhale and peak inhale breathing phase volumes. Finally we average the results obtained for all the supervoxel layers. Contours in images show lungs, ribs and main airways position. For illustrative purposes the supervoxels are extracted from a 2D image.

the centers are then corrected based on the gradients of the image to prevent their placement on image edges or at a noisy voxel. Individual voxels are assigned to the closest cluster based on the distance:

$$\mathcal{V} = \sqrt{(d_e)^2 + \left(\frac{d_I}{S}\right)^2 m^2}, \quad (5)$$

where m is a parameter setting the compactness of supervoxels, the distance \mathcal{V} is an iteratively calculated combination of Euclidean distance $d_e = \|\mathbf{x} - \mathbf{c}\|$ and the intensity-based similarity is $d_I = \|I(\mathbf{x}) - I(\mathbf{c})\|$, where \mathbf{x} is voxel position and \mathbf{c} are cluster centers updated after each iteration.

2.2. Supervoxel tracking for ventilation estimation

The existing methods [24, 36, 39, 58] for estimating ventilation from 4DCT take the structural relationship between voxels into account mainly at the image registration step or derivatives calculation. In this work we apply the proposed patch-based method, which additionally addresses structural relationship directly and estimates ventilation for larger, spatially and visually consistent regions. Such an approach may be more meaningful from an anatomical point of view. The lungs are divided into right and left lungs, which are further separated into lobes, while each lobe consists of a number of segments. All of them are supplied with separate airways which form a tree-like structure with no additional interconnections between the subtrees. Therefore, the ventilation of the neighboring lobes or sections supplied by different branches of the airway tree may differ. Supervoxels have the potential to cluster anatomically consistent lung regions and, therefore, ventilation surrogates would not be estimated across anatomical borders of the lungs.

285 In most of the previous studies ventilation images were estimated for peak
 286 exhale [58]. However in our work we used the peak inhale breathing phase
 287 as a reference, as the difference in the volume of the lungs between pMRI
 288 and CT was then the smallest. Such an approach should result in smaller
 289 deformations applied during pMRI to CT registration and, therefore more
 290 accurate results of the registration. A similar approach has been recently ap-
 291 plied in [28] to address the same challenges. We then formulate an estimate
 292 of the ventilation for peak inhale as follows:

$$Vent_{Dens}^{inh}(\mathbf{x}) = \left(\frac{HU_{exh}(\mathbf{x} + \mathbf{u}_{exh}) * G_{k1} - HU_{inh}(\mathbf{x}) * G_{k1}}{HU_{inh}(\mathbf{x}) * G_{k1} + 1000} \right) * G_{k2} \quad (6)$$

293 with $HU_{exh}(\mathbf{x})$ denoting the lung intensity value from peak exhale breathing
 294 phase image for voxel position \mathbf{x} and $HU_{inh}(\mathbf{x} + \mathbf{u}_{inh})$ lung intensity value from
 295 peak inhale breathing phase image for the same voxel moved by displacement
 296 field \mathbf{u}_{inh} and G_{k1}, G_{k2} are Gaussian kernels used for smoothing and convolved
 297 with the images. All the image intensities are given in HU.

298 We start by extracting supervoxels from the peak exhale breathing phase
 299 image and then calculate their mean intensities. Subsequently, we apply the
 300 deformations originating from image registration between peak exhale and
 301 peak inhale breathing volumes to the extracted supervoxels. In this way we
 302 map the same regions, represented by supervoxels, from the peak exhale to
 303 the peak inhale image (see Fig. 1). We recalculate mean intensities of the
 304 transformed supervoxels, this time over the peak inhale image. Then we ap-
 305 ply this approach to the method described above, thus estimating ventilation
 306 for supervoxels rather than for each individual voxel:

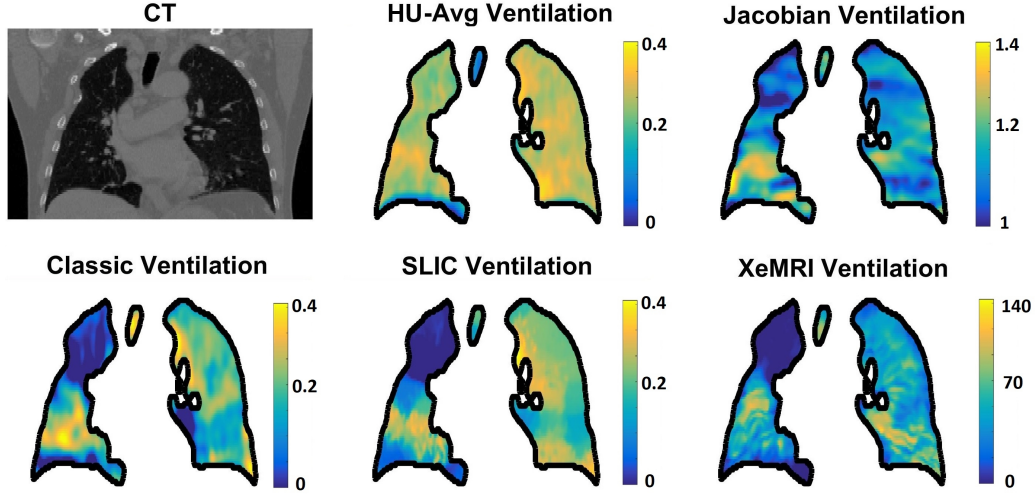


Figure 2: Comparison of the estimated ventilation maps using different methods for Patient 2 in coronal view. The results are presented for the supervoxel graph cuts image registration method. Lung contours extracted from the CT image are propagated onto ventilation images.

$$Vent_{SLIC}(\mathbf{s}) = \frac{\overline{HU_{exh}(\mathbf{s} + \mathbf{u}_{exh})} - \overline{HU_{inh}(\mathbf{s})}}{\overline{HU_{inh}(\mathbf{s})} + 1000}, \quad (7)$$

where $\overline{HU_{inh}(\mathbf{s})}$ is the mean intensity of a supervoxel \mathbf{s} extracted from peak
 inhale phase and $\overline{HU_{exh}(\mathbf{s} + \mathbf{u}_{exh})}$ stands for mean intensity of the same su-
 pervoxel \mathbf{s} mapped to peak exhale breathing phase by deformation \mathbf{u}_{exh} .
 Then all voxels belonging to the particular supervoxels are assigned the es-
 timated ventilation value from Eq. 7.

In the approach of [24, 58] (referenced to, henceforth, as ‘classic ap-
 proach’), described in Sec. 1, images are preprocessed using Gaussian filtering
 to compensate for mis-registration or other image artefacts. Therefore the
 ventilation of each voxel is influenced by all of its neighbors within a certain
 spatial distance. We propose to estimate the ventilation for groups of voxels

317 which are both spatially close and have similar intensity values. Such a for-
 318 mulation should more accurately correspond to anatomical structure of the
 319 lungs.

320 A particular clustering can have a strong influence on the results of the es-
 321 timated ventilation maps. As we do not put additional explicit constrains on
 322 the shape and size of the supervoxels, they might result in mis-segmentations.
 323 To address this issue, we propose to perform the extraction of a number of
 324 layers of supervoxels, akin to [18], where a similar approach has been ap-
 325 plied to deformable image registration. Such an approach has been shown
 326 to improve the robustness of the method, as well as reduce the influence of
 327 the particular clustering and the need to add further constrains to the clus-
 328 tering. Therefore we perform supervoxels clustering several times, each time
 329 changing slightly the initial clustering parameters, which results in different
 330 clusterings. Then the final estimated ventilation for a voxel is calculated as
 331 the average over all the layers of supervoxels:

$$\overline{Vent}_{SLIC} = \frac{1}{n} \sum_1^n Vent_{SLIC}^n, \quad (8)$$

332 where n is the number of layers of supervoxels. A visualization of the ven-
 333 tilation maps from both methods and XeMRI for Patient 2 is shown in Fig.
 334 2. To further improve the results, we apply Gaussian filtering with a small
 335 $[7 \ 7 \ 7]$ kernel and $\sigma = 1$ voxel over the final \overline{Vent}_{SLIC} .

336 2.3. XeMRI to CT alignment

337 In order to perform the evaluation of the correlation between 4DCT-
 338 based estimated ventilation maps and XeMRI ventilation images, we need to

bring these volumes into alignment. XeMRI ventilation images lack structural information. Therefore, their direct registration with CT would be an extremely challenging task. To address this issue we decided to first correct for the misalignment between XeMRI and pMRI with an affine registration method. Then we performed pMRI to CT registration. This task is thus divided into two steps: affine registration with mutual information as a similarity measure, which is followed by deformable registration with the use of deeds method [44].

3. Experiments and Results

We have conducted a number of experiments in which we have investigated different aspects of the estimated ventilation maps. We start from presenting in Sec. 3.1 materials on which we perform our experiments. In the following Sec. 3.2 and Sec. 3.3 we investigate the influence of the supervoxels size and the number of layers of supervoxels, respectively. Then, in Sec. 3.4 we calculate correlation coefficients between estimated ventilation maps and XeMRI. In Sec. 3.5 we evaluate the spatial overlap based on ventilation percentile ranges.

3.1. Materials

We performed the evaluation of the proposed method based on three cases (two male, one female, with ages ranging from 62 to 71 years old) consisting of 4DCT and XeMRI/pMRI data for patients undergoing radiotherapy treatment at Churchill Hospital in Oxford. The patients suffered from lung cancer stage II. The cancer staging for the patients was T2a-T3/4, N1-N2, and M0. 4DCT was acquired on a GE Optima CT580 RT scanner with phase sorting.

363 The patients lied supine on the couch with arms held above their head, and
 364 were coached on how to maintain regular tidal breathing. A mixture of ^{129}Xe
 365 gas (80%) and air was polarized on-site to between 4% and 12%, by using
 366 a commercial polarizer (Model 1651; GE Healthcare, Milwaukee, Wisconsin,
 367 USA) operating on the rubidium vapor spin-exchange optical pumping ba-
 368 sis, and deposited in a Tedlar bag (Jensen Inert Products, Coral Springs,
 369 Florida, USA). Hyperpolarized ^{129}Xe was administered by first instructing
 370 the subjects, who were lying supine in the MR imaging unit, to exhale to
 371 Functional Residual Capacity (FRC) and then inhale the 1.0 liter contents
 372 of the Tedlar bag through 9.5mm inner diameter Tygon tubing (Cole-Palmer
 373 Instrument; Hanwell, London, UK). Subjects were then instructed to hold
 374 their breath for up to 25 seconds for image acquisition [65]. The pMRI and
 375 XeMRI scans were obtained with a 1.5-T whole-body system (Signa HDx;
 376 GE Healthcare). The spatial resolution of the XeMRI/pMRI is $1.56 \times 1.56 \times 20$
 377 mm^3 , whereas for CT it is $0.977 \times 0.977 \times 2.5 \text{ mm}^3$. All data were resampled to
 378 an isotropic resolution of $1 \times 1 \times 1 \text{ mm}^3$ size. The sequence of 4DCT consisted
 379 of 10 volumes of different breathing phases. Due to the rarity of the data
 380 and the limited number of available datasets, we could not create separate
 381 training and testing datasets. In the presented study, we chose one random
 382 dataset to ~~fine~~ pre-tune the parameters of the proposed method and then
 383 fixed them for the other two. This process was repeated three times, for each
 384 of the cases. In such a way we found Gaussian kernel parameters and initial
 385 settings for the size of the supervoxels. During this procedure we used only
 386 one image registration method: deeds, fixed for all the cases.

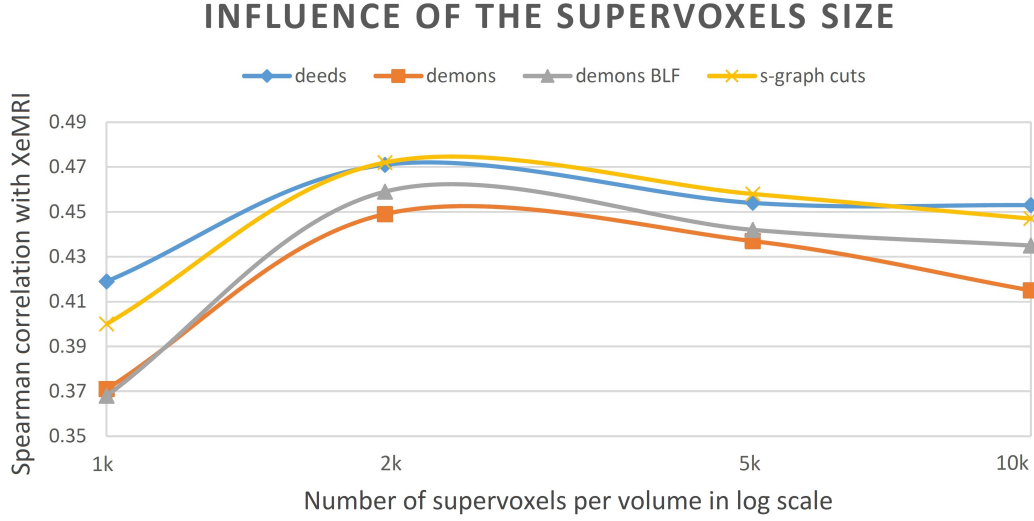


Figure 3: The plot shows the influence of the size of the supervoxels on the correlation of the estimated ventilation maps for all four registration methods with XeMRI ventilation images. The x-axis with supervoxel size is shown on a logarithmic scale. It is noticeable that for a low number of supervoxels the correlation is relatively low, then it reaches its maximum at approximately 2,000 supervoxels. The correlation gradually decays or reaches the plateau after further increasing the number of supervoxels.

3.2. Influence of the supervoxel size

The size of the supervoxels is one of the factors that have an influence on the results of the estimated ventilation maps. On the one hand, supervoxels that are too large may not be capable of modeling the regional nature of the ventilation changes. On the other hand, if too small, the supervoxels might lose their structure-oriented properties and provide similar results to the voxel-wise approaches. The purpose of this experiment is to investigate how the size of the supervoxels influences the correlation of the estimated ventilation maps with XeMRI ventilation images, and if there is a local maximum indicating an optimal size of the supervoxels. To investigate these properties, we have measured the correlation of the SLIC-based

398 estimated ventilation maps with XeMRI using different supervoxel sizes. We
 399 have extracted approximately 1,000, 2,000, 5,000 and 10,000 of supervoxels
 400 from each volume. The experiments were conducted with a fixed number of
 401 supervoxel layers, namely 15, which is a reasonable trade-off between per-
 402 formance and computational requirements. We have performed the same
 403 experiment for all of the registration methods. In Fig. 3 we present a plot
 404 showing the trend for average results on a logarithmic scale. The detailed
 405 results for each individual case are presented in Appendix A.

406 For a sparse image representation with a low number of large supervox-
 407 els, the results show relatively poor correlation with XeMRI. However, by
 408 increasing the number of supervoxels, and hence, reducing their size, we find
 409 that the correlation reaches its maximum for approximately 2,000 supervox-
 410 els extracted from a volume. Results gradually decay for increasing number
 411 of supervoxels of decreasing size. All image registration methods exhibit a
 412 similar trend in their correlation with XeMRI.

413 *3.3. Influence of the number of layers*

414 The number of layers of supervoxels has an obvious influence on the esti-
 415 mated ventilation images. Using just a single layer of supervoxels, the results
 416 might be biased by the particular image clustering. By applying a larger
 417 number of layers, the results should be more robust and we would expect the
 418 correlation with XeMRI to be higher. We conducted an experiment investi-
 419 gating the influence of the number of layers of supervoxels on the correlation
 420 between the estimated ventilation maps with XeMRI for all four image regis-
 421 tration methods. We estimated ventilation maps for 1, 5, 10, 15 and 25 layers
 422 of supervoxels. The size of the supervoxels was adjusted based on the previ-

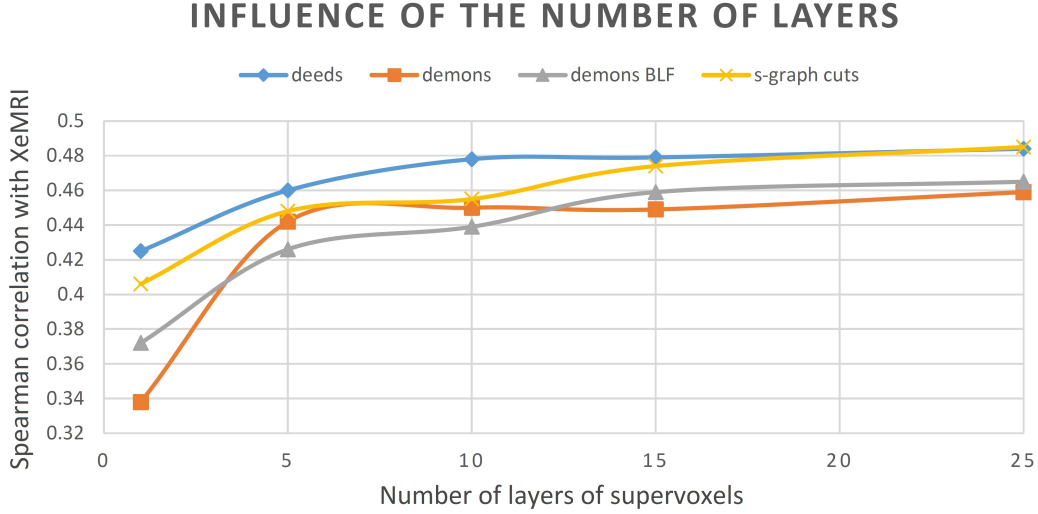


Figure 4: The plot shows the influence of the number of supervoxel layers on the correlation of the estimated ventilation maps with XeMRI ventilation images for all four registration methods. The correlation improves when the number of layers is increased, reaching a plateau for 25 layers.

ous experiment to approximately 2k supervoxels per volume. The obtained
 average results are shown in Fig. 4. The detailed results for each individual
 case are presented in Appendix B. The proposed method achieves relatively
 low correlation when there is just one layer of supervoxels. The results im-
 prove noticeably after increasing the number of layers to 5 layers, while there
 is a more gradual improvement up to 15. With the use of more than 15
 layers of supervoxels the correlation between XeMRI and the investigated
 ventilation surrogates estimated using different image registration methods
 reaches a plateau, with only slight improvement for 25 layers. Similar trends
 can be observed independently of the applied registration method.

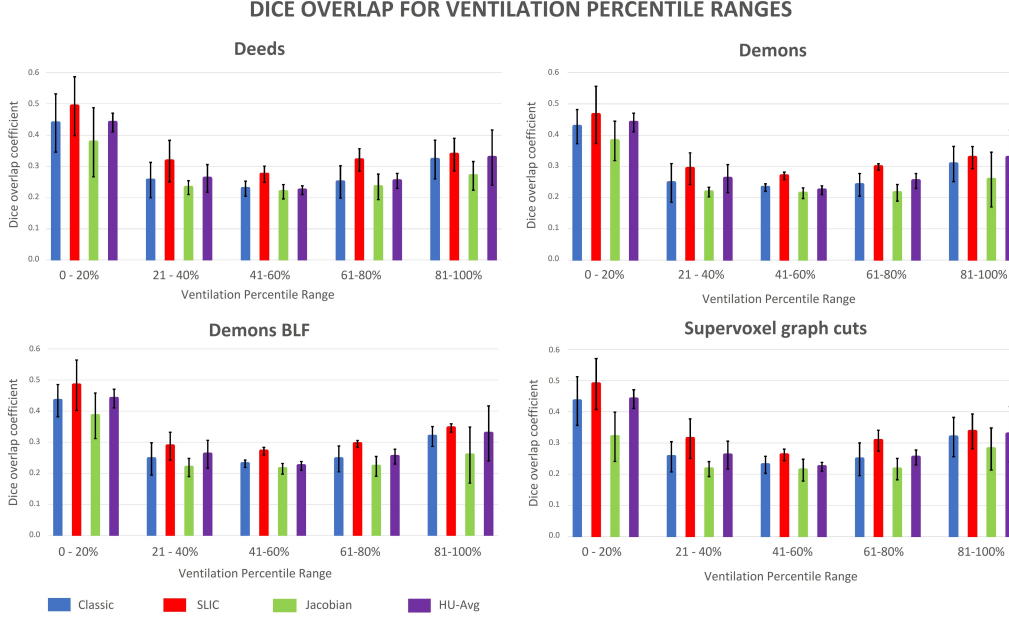


Figure 5: Dice overlap coefficient calculated for masks created based on the ventilation percentile ranges. We investigate the results for all four image registration methods: deeds, demons, demons with BLF and supervoxel graph cuts. For each of them we calculate all four estimates of the ventilation. We present average results for all three patients from our dataset. The highest Dice overlap was achieved for the proposed method in red. It can be noticed that similar patterns in the results can be observed for all of the tested image registration methods.

3.4. Global correlation

To investigate the global relation of the estimated ventilation maps with XeMRI we calculate Spearman’s correlation coefficient for all methods: the classic intensity based [24, 38], the proposed SLIC-based, Jacobian based [36, 37] and HU averaging [39]. Despite the fact that the classic intensity based, Jacobian based and HU averaging methods were not initially developed for the evaluation on hyperpolarized gas MRI, they have been successfully used to study and compare ventilation surrogates with this ventilation

Table 1: Spearman’s correlation coefficients calculated for all ventilation estimation methods. For the classic methods, SLIC-based and Jacobian-based we present results achieved by investigated image registration methods. In the case of HU-Avg no image registration method was applied. The highest correlations have been achieved for the proposed SLIC-based method.

	Classic				SLIC				Jacobian				HU-Avg
Pat. no.	demons	demons BLF	deeds	graph cuts	demons	demons BLF	deeds	graph cuts	demons	demons BLF	deeds	graph cuts	no reg.
1	0.205	0.306	0.356	0.348	0.369	0.426	0.476	0.477	0.274	0.273	0.280	0.278	0.399
2	0.605	0.598	0.645	0.633	0.667	0.656	0.690	0.678	0.335	0.349	0.414	0.339	0.444
3	0.279	0.256	0.186	0.198	0.332	0.313	0.287	0.299	0.096	0.105	0.109	0.101	0.315
Avg	0.363	0.386	0.396	0.393	0.459	0.465	0.484	0.485	0.235	0.242	0.268	0.231	0.386

imaging method [26, 28]. For all these methods we have used $G_{k1} = G_{k2}$ with [15 15 15] voxel kernels size and $\sigma = 2$ voxels, as these settings have been previously reported in the literature [28, 39], and were shown to reach plateau in terms of correlation with hyperpolarized gas MRI ventilation [28]. Only from the proposed SLIC-based method we applied a smaller, [7 7 7] voxel kernel size filter with $\sigma = 1$ voxel. We refer an interested reader on the influence of the applied filter sizes on the correlation of the ventilation surrogates with hyperpolarized gas MRI to, for instance, [28]. The image registration methods used to estimate the deformations for ventilation surrogates were applied with the parameters optimized by their authors when evaluated on Dir-Lab dataset [52].

In this experiment, we achieved a higher correlation for our method compared with the others, when applied voxel-wise manner on average for all cases. The best results were obtained independently of the chosen image registration method. The classic approach achieved higher correlation compared with HU averaging method for all image registration methods, apart from the classic demons method. The lowest correlations with XeMRI were

458 obtained for the Jacobian-based method for all registration methods. Only
459 for this ventilation estimation approach, demons BLF achieved higher corre-
460 lation than supervoxel graph cuts for one of the cases, yet still lower than the
461 deeds method. The numerical results are presented in Table 1. Visualization
462 of the estimated ventilation maps for one of the cases is shown in Fig. 2.

463 The visualization of the results is presented in Fig. 6 for all cases. We also
464 calculate correlation between the proposed ventilation estimation method
465 and the classic, showing that they correlate well (0.834), with the proposed
466 method achieving the best correlation with XeMRI.

467 Worth noticing is relatively high correlation achieved by the HU-Avg
468 method. The method has failed to provide local estimates of the ventilations,
469 resulting in a blurred image of the shape of the lungs. Such an explanation
470 can be confirmed by a closer investigation of the visual results in Fig. 2
471 where the ventilation surrogates for one of the patients are presented. Similar
472 behavior was observed throughout the dataset. In our experiments we could
473 hardly observe local patterns of the ventilation changes. We also could not
474 see the trend visible for other methods where the results of the correlation
475 with XeMRI for patient 2 were noticeably higher than for the other two.

476 For Jacobian-based ventilation the results obtained by different image
477 registration methods are more consistent than for the classic and SLIC-based,
478 especially for patient 1 and 3.

479 3.5. *Spatial overlap comparison*

480 We have performed a series of experiments investigating the quantitative
481 relation between the spatial distribution of the estimated ventilation maps
482 and XeMRI ventilation images. Akin to [59], we have divided the estimated

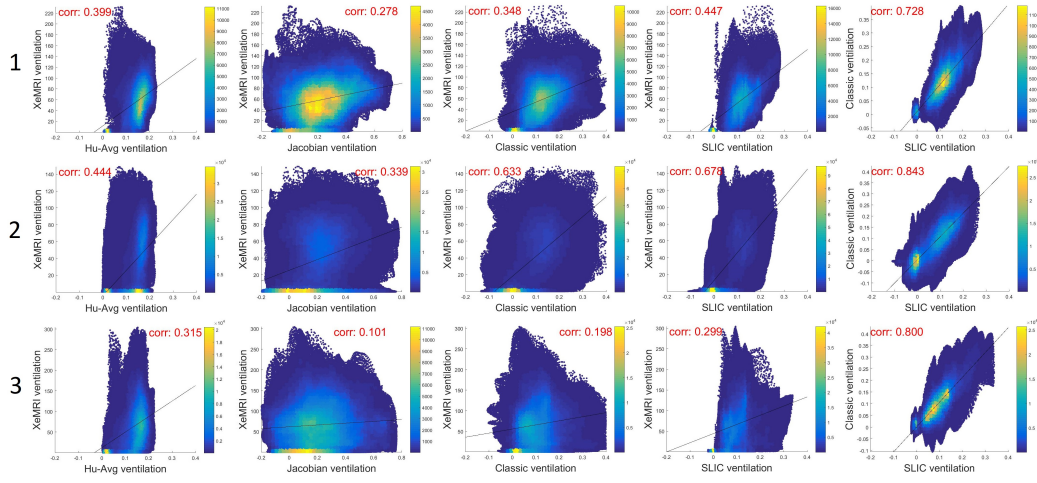


Figure 6: The figure shows correlation and Spearman correlation coefficient between the HU averaging ventilation approach and XeMRI in the first column. In the second column, correlation and Spearman correlation coefficient between the Jacobian-based ventilation approach and XeMRI are presented. In the following columns analogical correlations are presented for the classic approach and for the proposed SLIC-based method. In the last column, correlation between the classic and the proposed method are shown. Rows correspond to patient's number.

483 ventilation images into five disjoint regions, based on calculated percentile
484 distribution ranges. These regions were further used to create masks corre-
485 sponding to the percentile ranges. For each of them, we calculated the Dice
486 overlap coefficient with corresponding masks of XeMRI. We have applied this
487 procedure to all four lung ventilation estimation methods and repeated the
488 experiments for all investigated image registration approaches.

489 The visualization of the results is presented in Fig. 5. The general trend,
490 where Dice overlap is the highest for the first percentile range (0-20%), for the
491 intermediate ranges is lower, and then raises for the last percentile range (81-
492 100%) is in agreement with similar experiments in the literature [59]. Similar
493 patterns in the results can be observed for all of the tested image registration
494 methods. For all of the evaluated percentile ranges, the highest correlation
495 has been achieved for our proposed method (in red). The lowest Dice overlap
496 has been obtained for the Jacobian-based ventilation method. The classic
497 approach and HU averaging method achieved similar results. The results for
498 the HU averaging method are independent of the image registration methods.
499 However, we decided to include them in the plots showing the results of the
500 correlation for different image registration methods to enable the comparison
501 with them.

502 4. Discussion and Conclusions

503 In this work, we have introduced and investigated the patch-based ap-
504 proach for ventilation estimation. We have conducted a number of exper-
505 iments, measuring the correlation of the estimated ventilation maps with
506 XeMRI ventilation images. To perform this evaluation, we have proposed

507 a registration framework to bring SLIC-based ventilation images into align-
508 ment with XeMRI. The presented results show that the proposed method
509 results in higher correlation with XeMRI for a number of performed tests.

510 We have investigated the influence of the supervoxel size in Sec. 3.2 for
511 all of the image registration methods. In the results presented in Fig. 3 we
512 can observe that to achieve the best correlation the size of the supervoxel
513 needs to be chosen with care. In our experiments we have found out that the
514 highest correlation has been achieved for approximately 2,000 supervoxels per
515 volume. This means that the average supervoxel consists of 30,000 isotropic
516 $1 \times 1 \times 1 \text{ mm}^3$ voxels. This is related to their ability to model the anatomy of
517 the lungs. This trend in the changes of correlation has been expected and
518 supports our claim that structure-oriented patch-based approach is a better
519 choice than a voxel-wise approach. The limited number of available cases did
520 not allow us to create separate training and testing datasets. Apart from the
521 image registration methods settings, all other parameters of the presented
522 ventilation estimation method were trained and tested ~~on~~ with the use of the
523 available dataset ~~of three cases~~ in a manner described in Materials section.
524 The chosen approach might be seen as suboptimal, however due to the unique
525 character of the dataset, creation of the separate training and testing datasets
526 based on them was not feasible. Further evaluation on the larger dataset
527 would be required to draw meaningful conclusions about superiority of the
528 proposed method compared to other approaches. .

529 The results from Sec. 3.3 show that a larger number of layers of super-
530 voxels provides images more correlated with XeMRI. This is expected, as
531 a larger number of layers of supervoxels should improve the robustness of

532 the method for mis-segmentations originating from a particular supervoxel
533 extraction. In our work we have not investigated the influence of the com-
534 pactness of supervoxels because the intention is for the supervoxels to mimic
535 the anatomy of the lungs. Therefore, this parameter was adjusted manually
536 to make the supervoxels correspond in shape to lung structures.

537 When investigating the influence of the number of supervoxels on the cor-
538 relation between XeMRI and ventilation surrogates, we have applied a num-
539 ber of different image registration methods. Despite differences in approaches
540 of the studied methods, we have observed a similar trend of the correlation
541 for all of them. This observation suggests that the proposed method is not
542 restricted to one of the evaluated methods, but is more universal, as the
543 methods investigated in our study represent the main registration categories
544 in terms of optimization, namely: discrete, continuous, and hybrid. Given
545 the small number of cases analysed, we cannot provide a definitive answer
546 as to whether the registration methods are equivalent; however, we believe
547 the similarity of the results provides some reassurance as to the robustness
548 of the method in this respect.

549 The results presented in Sec. 3.4, where the classic demons image reg-
550 istration method was compared with its sliding motion preserving version,
551 show that the incorporation of the sliding motion improves the correlation of
552 the estimated ventilation maps with XeMRI. This observation supports the
553 claim that sliding motion preservation results in more anatomically plausi-
554 ble deformations of the registration. The deeds [44] and supervoxel graph
555 cuts [46] methods showed slightly more accurate performance on the Dir-Lab
556 dataset [52] than both demons methods, which is also reflected in the higher

557 correlations calculated for these methods. The difference between the cor-
558 relations calculated for the deeds [44] and supervoxel graph cuts [46] for all
559 ventilation estimation methods is minimal (below 0.01). This might suggest
560 that even though both methods represent different approaches to the image
561 registration problem, both cope well with the task providing similar level of
562 accuracy. This also suggests that more accurate image registration methods
563 provide estimations of ventilation which result in higher levels of correlation
564 with XeMRI.

565 The analysis of the Dice overlap for the ventilation percentile ranges
566 shows favorable performance of our method for all investigated ranges. The
567 Jacobian-based ventilation maps resulted in lower correlation with XeMRI
568 than the classic approach. This observation is in agreement with previous
569 findings from [58]. An interesting observation is that the HU averaging meth-
570 ods achieves comparable results to the classic approach. Especially in the
571 context of the results reported in [39], where the authors found low correla-
572 tion for the patients with severe ventilation defects, which is also the case in
573 our study.

574 In our work we have investigated the influence on the correlation of the
575 estimated ventilation with XeMRI of using four different image registration
576 methods. They represent distinct approaches to the task, covering most of
577 the existing groups of methods. We did not aim to evaluate which of the regis-
578 tration methods performed best, but rather wanted to show the general trend
579 that the application of our supervoxel-based ventilation estimation improves
580 the correlation to XeMRI ventilation maps, irrespective of the underlying
581 image registration.

582 An open point for a discussion might be whether the achieved level of
 583 correlation reaches the expectations and is applicable to enhance radiother-
 584 apy. The proposed SLIC-based method and the classic approach were able
 585 to identify severe ventilation defects, as shows an example in Fig. 2. Precise
 586 localization of the ventilation defects remains challenging to evaluate. In a
 587 recent study [66], the researchers have evaluated and compared ventilation
 588 maps estimated on 4DCT and high quality exhale/inhale breath-hold CT
 589 (BHCT) with Galligas PET. They found that ventilation maps estimated
 590 using BHCT achieved higher correlation values. Such an observation may be
 591 mainly due to reconstruction artifacts present in 4DCT, and could suggest
 592 that the application of BHCT has the potential to improve the accuracy of
 593 the estimated ventilation maps. Additionally, in our opinion an improved
 594 pMRI to CT registration, which brings XeMRI to the alignment with CT,
 595 plays an important role in this evaluation. The method applied in our study,
 596 as well as methods applied by other researchers were not developed strictly
 597 for this task. Therefore, the pattern of the regularization applied inside of
 598 the lungs might not be fully corresponding with the anatomy of the lungs.

599 A detailed analysis including a larger group of patients could further
 600 support our results. The presented results, where for the majority of the
 601 conducted experiments the proposed method for ventilation estimation from
 602 4DCT achieves better correlations with XeMRI images, indicate higher phys-
 603 iological consistency of our proposed approach using supervoxels for ventila-
 604 tion estimation. In future, we are planning to perform further analysis on
 605 a larger patient group. Another crucial issue is XeMRI to CT registration.
 606 We could observe the improvement in the correlation for more accurate im-

age registration methods. We would expect further improvements when task dedicated registration between pMRI and CT was applied. Due to a limited amount of information on inner lung structure in pMRI, the standard image registration methods might be suboptimal for this task and dedicated frameworks could potentially provide more accurate results [67].

We have presented a proof of concept for a patch-based ventilation estimation method from 4DCT. We have shown that our proposed method achieves higher correlation coefficients compared to the classic approach when correlated with XeMRI. The results, already encouraging at the current stage, would gain on significance when evaluated on a larger cohort of patients , where separate training and testing datasets would be applied.

Conflict of interest

The authors have no conflict of interest to disclose.

Acknowledgements

A.S. and B.W.P. would like to acknowledge funding from the CRUK and EPSRC Cancer Imaging Centre in Oxford. B.W.P. acknowledges Oxford NIHR Biomedical Research Centre (Rutherford Fund Fellowship at HDR UK). We would also like to acknowledge M. Heinrich for making his code for the deeds image registration method [44] available online.

626 **References**

- 627 [1] B. Fulkerson, A. Vedaldi, S. Soatto, Class segmentation and object
628 localization with superpixel neighborhoods, *IEEE Int. Conf. Comput.*
629 *Vis.* (2009) 670–677.
- 630 [2] H. Kim, S. Lee, D. Lee, S. Choi, J. Ju, H. Myung, Real-time human pose
631 estimation and gesture recognition from depth images using superpixels
632 and svm classifier, *Sensors* 15 (2015) 12410–12427.
- 633 [3] C. L. Zitnick, S. B. Kang, Stereo for image-based rendering using image
634 over-segmentation, *Int. J. Comput. Vision* 75 (2007) 49–65.
- 635 [4] B. Liu, S. Gould, D. Koller, Single image depth estimation from pre-
636 dicted semantic labels, *Comput. Vis. Pattern Recognit.* (2010) 1253–
637 1260.
- 638 [5] D. G. Lowe, Object recognition from local scale-invariant features 40
639 (1999) 1150–.
- 640 [6] E. Tola, V. Lepetit, P. Fua, Daisy: An efficient dense descriptor applied
641 to wide-baseline stereo, *IEEE Transactions on Pattern Analysis and*
642 *Machine Intelligence* 32 (2010) 815–830.
- 643 [7] E. Shechtman, M. Irani, Matching local self-similarities across images
644 and videos, *IEEE Conference on Computer Vision and Pattern Recogni-*
645 *tion* (2007).
- 646 [8] A. Lucchi, K. Smith, R. Achanta, G. Knott, P. Fua, Supervoxel-based

- 647 segmentation of mitochondria in em image stacks with learned shape
648 features, *IEEE Transactions on Medical Imaging* 31 (2012) 474–486.
- 649 [9] D. Mahapatra, P. J. Schffler, J. A. W. Tielbeek, J. C. Makanyanga,
650 J. Stoker, S. A. Taylor, F. M. Vos, J. M. Buhmann, Automatic detection
651 and segmentation of crohn’s disease tissues from abdominal mri, *IEEE*
652 *Transactions on Medical Imaging* 32 (2013) 2332–2347.
- 653 [10] W. Chen, M. Giger, U. Bick, A fuzzy c-means (fcm)-based approach
654 for computerized segmentation of breast lesions in dynamic contrast-
655 enhanced mr images1 13 (2006) 63–72.
- 656 [11] B. Irving, J. Franklin, B. W. Papiez, E. Anderson, R. Sharma,
657 F. V. Gleeson, M. Brady, J. Schnabel, Pieces-of-parts for supervoxel
658 segmentation with global context: Application to dce-mri tumour delin-
659 eation 32 (2016) 69–83.
- 660 [12] P. Su, J. Yang, H. Li, L. Chi, Z. Xue, S. T. Wong, Superpixel-based
661 segmentation of glioblastoma multiforme from multimodal mr images,
662 *Multimodal Brain Image Analysis* (2013) 74–83.
- 663 [13] H. Winter, J. Mirecka, B. Papiez, B. Irving, M. Jenkinson, M. Chappell,
664 R. A. Sharma, J. Schnabel, Clinical feasibility of texture analysis in dce
665 mri of patients receiving selective internal radiation therapy, *European*
666 *Journal of Surgical Oncology* 44 (2018) S30 – S31.
- 667 [14] Y. Zhang, G. Wu, P.-T. Yap, Q. Feng, J. Lian, W. Chen, D. Shen, Hier-
668 archical patch-based sparse representationa new approach for resolution

- enhancement of 4d-ct lung data, *IEEE transactions on medical imaging*
31 (2012) 1993–2005.
- [15] M. P. Heinrich, M. Jenkinson, M. Bhushan, T. Martin, F. V. Gleeson,
M. Brady, J. A. Schnabel, MIND: modality independent neighbourhood
descriptor for multi-modal deformable registration., *Med Image Anal*
16 (2012) 1423–35.
- [16] A. Hallack, B. W. Papież, J. Wilson, L. M. Wang, T. Maughan, M. J.
Gooding, J. A. Schnabel, Correlating tumour histology and ex vivo
mri using dense modality-independent patch-based descriptors (2015)
137–145.
- [17] M. Kim, G. Wu, Q. Wang, S.-W. Lee, D. Shen, Improved image regis-
tration by sparse patch-based deformation estimation, *NeuroImage* 105
(2015) 257 – 268.
- [18] M. P. Heinrich, I. J. Simpson, B. W. Papież, S. M. Brady, J. A. Schnabel,
Deformable image registration by combining uncertainty estimates from
supervoxel belief propagation, *Med. Image Anal.* 27 (2016) 57–71.
- [19] A. Szmul, B. W. Papież, R. Bates, A. Hallack, J. A. Schnabel, V. Grau,
Graph Cuts-Based Registration Revisited: A Novel Approach for Lung
Image Registration Using Supervoxels and Image-Guided Filtering,
Comput. Vis. Pattern Recognit. Workshops (CVPRW) (2016) 592–599.
- [20] C. J. L. Murray, Global, regional, and national age-sex specific all-
cause and cause-specific mortality for 240 causes of death, 1990-2013: a

- 691 systematic analysis for the Global Burden of Disease Study 2013, *Lancet*
692 385 (2015) 117–171.
- 693 [21] J. Ferlay, H. Shin, F. Bray, D. Forman, C. Mathers, D. Parkin, Cancer
694 incidence and mortality worldwide: Iarc cancerbase no 2 (2013).
- 695 [22] L. B. Herpel, et al., Variability of spirometry in chronic obstructive
696 pulmonary disease: results from two clinical trials., *American journal*
697 *of respiratory and critical care medicine* 173 (2006) 1106–1113.
- 698 [23] E. J. Sims, D. Price, Spirometry: an essential tool for screening, case-
699 finding, and diagnosis of COPD, *Prim Care Respir J* 21 (2012) 128–130.
- 700 [24] T. Guerrero, K. Sanders, J. Noyola-Martinez, E. Castillo, Y. Zhang,
701 R. Tapia, R. Guerra, Y. Borghero, R. Komaki, Quantification of re-
702 gional ventilation from treatment planning ct, *International Journal of*
703 *Radiation Oncology*Biophysics* 62 (2005) 630 – 634.
- 704 [25] R. H. Ireland, B. A. Tahir, J. M. Wild, C. E. Lee, M. Q. Hatton, Func-
705 tional Image-guided Radiotherapy Planning for Normal Lung Avoid-
706 ance, *Clinical Oncology* 28 (2016) 695–707.
- 707 [26] L. Mathew, A. Wheatley, R. Castillo, E. Castillo, G. Rodrigues, T. Guer-
708 rero, G. Parraga, Hyperpolarized ^3He magnetic resonance imaging: com-
709 parison with four-dimensional x-ray computed tomography imaging in
710 lung cancer, *Academic radiology* 19 (2012) 1546–1553.
- 711 [27] B. A. Tahir, C. Van Holsbeke, R. H. Ireland, A. J. Swift, F. C. Horn,
712 H. Marshall, J. C. Kenworthy, J. Parra-Robles, R. Hartley, R. Kay,

- et al., Comparison of ct-based lobar ventilation with 3he mr imaging ventilation measurements, *Radiology* 278 (2015) 585–592.
- [28] B. Tahir, P. Hughes, S. Robinson, H. Marshall, N. Stewart, G. Norquay, A. Biancardi, H.-F. Chan, G. Collier, K. Hart, et al., Spatial comparison of ct-based surrogates of lung ventilation with hyperpolarized helium-3 and xenon-129 gas mri in patients undergoing radiation therapy, *International Journal of Radiation Oncology Biology Physics* (2018).
- [29] L. J. Rankine, Z. Wang, B. Driehuys, L. B. Marks, C. R. Kelsey, S. K. Das, Correlation of regional lung ventilation and gas transfer to red blood cells: Implications for functional-avoidance radiation therapy planning, *International Journal of Radiation Oncology Biology Physics* (2018).
- [30] A. Szmul, B. W. Papież, T. Matin, F. V. Gleeson, J. A. Schnabel, V. Grau, Regional lung ventilation estimation based on supervoxel tracking, *SPIE Medical Imaging* 10576 (2018) 10576 – 10576 – 7.
- [31] P. J. Roach, D. J. Gradinscak, G. P. Schembri, E. A. Bailey, K. P. Willowson, D. L. Bailey, Spect/ct in v/q scanning, *Seminars in Nuclear Medicine* 40 (2010) 455 – 466.
- [32] S. Siva, R. Thomas, J. Callahan, N. Hardcastle, D. Pham, T. Kron, R. J. Hicks, M. P. MacManus, D. L. Ball, M. S. Hofman, High-resolution pulmonary ventilation and perfusion PET/CT allows for functionally adapted intensity modulated radiotherapy in lung cancer, *Radiotherapy and Oncology* 115 (2015) 157–162.

- 736 [33] M. S. Albert, G. D. Cates, B. Driehuys, W. Happer, B. Saam, C. S.
737 Springer, A. Wishnia, Biological magnetic resonance imaging using
738 laser-polarized ^{129}Xe , *Nature* 370 (1994) 199–201.
- 739 [34] J. P. Mugler, T. A. Altes, Hyperpolarized ^{129}Xe MRI of the human
740 lung., *J Magn Reson Imaging* 37 (2013) 313–31.
- 741 [35] O. Doganay, T. N. Martin, A. McIntyre, B. Burns, R. F. Schulte, F. Glee-
742 son, D. P. Bulte, Fast dynamic ventilation mri of hyperpolarized ^{129}Xe
743 using spiral imaging, *Magnetic resonance in medicine* (2017).
- 744 [36] J. M. Reinhardt, G. E. Christensen, E. A. Hoffman, K. Ding, K. Cao,
745 Registration-derived estimates of local lung expansion as surrogates for
746 regional ventilation, in: *Information Processing in Medical Imaging*, pp.
747 763–774.
- 748 [37] J. M. Reinhardt, K. Ding, K. Cao, G. E. Christensen, E. A. Hoffman,
749 S. V. Bodas, Registration-based estimates of local lung tissue expansion
750 compared to xenon ct measures of specific ventilation, *Medical Image*
751 *Analysis* 12 (2008) 752 – 763.
- 752 [38] T. Yamamoto, S. Kabus, T. Klinder, C. Lorenz, J. von Berg, T. Blaf-
753 fert, B. W. Loo, P. J. Keall, Investigation of four-dimensional computed
754 tomography-based pulmonary ventilation imaging in patients with em-
755 physematous lung regions., *Phys. Med. Biol.* 56 (2011) 2279–98.
- 756 [39] J. Kipritidis, M. Hofman, S. Siva, J. Callahan, P.-Y. Le Roux,
757 H. Woodruff, W. Counter, P. Keall, Estimating lung ventilation directly
758 from 4d ct hounsfield unit values 43 (2016) 33–43.

- 759 [40] D. Rueckert, L. I. Sonoda, C. Hayes, D. L. Hill, M. O. Leach, D. J.
760 Hawkes, Nonrigid registration using free-form deformations: application
761 to breast MR images., *IEEE Trans. Med. Imag* 18 (1999) 712–21.
- 762 [41] B. W. Papież, M. P. Heinrich, J. Fehrenbach, L. Risser, J. A. Schn-
763 abel, An implicit sliding-motion preserving regularisation via bilateral
764 filtering for deformable image registration., *Med. Image Anal.* 18 (2014)
765 1299–311.
- 766 [42] L. Risser, F. X. Vialard, H. Y. Baluwala, J. A. Schnabel, Piecewise-
767 diffeomorphic image registration : application to the motion estimation
768 between 3D CT lung images with sliding conditions, *Med Image Anal*
769 17 (2013) 182–193.
- 770 [43] J. Rühaak, T. Polzin, S. Heldmann, I. J. A. Simpson, H. Handels,
771 J. Modersitzki, M. P. Heinrich, Estimation of Large Motion in Lung
772 CT by Integrating Regularized Keypoint Correspondences into Dense
773 Deformable Registration 0062 (2017).
- 774 [44] M. P. Heinrich, M. Jenkinson, M. Brady, J. A. Schnabel, MRF-based
775 deformable registration and ventilation estimation of lung CT., *IEEE*
776 *Trans. Med. Imag.* 32 (2013) 1239–1248.
- 777 [45] J.-P. Thirion, Image matching as a diffusion process: An analogy with
778 maxwell’s demons 2 (1998).
- 779 [46] A. Szmul, B. W. Papież, A. Hallack, V. Grau, J. A. Schnabel, Super-
780 voxels for graph cuts-based deformable image registration using guided
781 image filtering, *Journal of Electronic Imaging* 26 (2017) 26 – 26 – 13.

- 782 [47] T. Vercauteren, X. Pennec, A. Perchant, N. Ayache, Non-parametric
783 diffeomorphic image registration with the demons algorithm., MICCAI
784 10 (2007) 319–326.
- 785 [48] C. Tomasi, R. Manduchi, Bilateral filtering for gray and color images.,
786 Proceedings of the Sixth International Conference on Computer Vision
787 (ICCV- 98) (1998) 839–846.
- 788 [49] Y. Boykov, O. Veksler, R. Zabih, Fast approximate energy minimization
789 via graph cuts, IEEE Trans. Pattern Anal. Mach. Intell. 23 (2001) 1222–
790 1239.
- 791 [50] K. He, J. Sun, X. Tang, Guided Image Filtering, IEEE Trans. Pattern
792 Anal. Mach. Intell. 35 (2013) 1397–1409.
- 793 [51] B. W. Papież, J. Franklin, M. P. Heinrich, F. V. Gleeson, J. A. Schn-
794 abel, Liver motion estimation via locally adaptive over-segmentation
795 regularization, in: Medical Image Computing and Computer-Assisted
796 Intervention – MICCAI 2015, Springer International Publishing, 2015,
797 pp. 427–434.
- 798 [52] R. Castillo, E. Castillo, R. Guerra, V. E. Johnson, T. McPhail, A. K.
799 Garg, T. Guerrero, A framework for evaluation of deformable image
800 registration spatial accuracy using large landmark point sets., Phys.
801 Med. Biol. 54 (2009) 1849–1870.
- 802 [53] A. Sotiras, C. Davatzikos, N. Paragios, Deformable medical image reg-
803 istration: a survey, IEEE Trans. Med. Imag 32 (2013) 1153–1190.

- 804 [54] J. A. Schnabel, M. P. Heinrich, B. W. Papież, S. M. Brady, Advances
805 and challenges in deformable image registration: From image fusion to
806 complex motion modelling., *Med. Image Anal.* 33 (2016) 145–148.
- 807 [55] Y. Yin, E. a. Hoffman, C.-L. Lin, Mass preserving nonrigid registration
808 of CT lung images using cubic B-spline., *Medical physics* 36 (2009)
809 4213–4222.
- 810 [56] V. Gorbunova, J. Sporring, P. Lo, M. Loeve, H. A. Tiddens, M. Nielsen,
811 A. Dirksen, M. de Bruijne, Mass preserving image registration for lung
812 CT, *Med Image Anal* 16 (2012) 786–795.
- 813 [57] B. W. Papież, A. Szmul, V. Grau, J. M. Brady, J. A. Schnabel, Non-local
814 graph-based regularization for deformable image registration (2016)
815 199–207.
- 816 [58] T. Yamamoto, S. Kabus, T. Klinder, J. von Berg, C. Lorenz, B. W.
817 Loo, P. J. Keall, Four-dimensional computed tomography pulmonary
818 ventilation images vary with deformable image registration algorithms
819 and metrics., *Med. Phys.* 38 (2011) 1348–1358.
- 820 [59] R. Castillo, E. Castillo, J. Martinez, T. Guerrero, Ventilation from Four
821 Dimensional Computed Tomography: Density versus Jacobian Methods,
822 *Medical Physics* 55 (2010) 4661–4685.
- 823 [60] J. Kipritidis, S. Siva, M. S. Hofman, J. Callahan, R. J. Hicks, P. J.
824 Keall, Validating and improving ct ventilation imaging by correlating
825 with ventilation 4d-pet/ct using 68ga-labeled nanoparticles, *Medical*
826 *physics* 41 (2014).

- 827 [61] K. Du, J. E. Bayouth, K. Ding, G. E. Christensen, K. Cao, J. M. Rein-
828 hardt, Reproducibility of intensity-based estimates of lung ventilation,
829 Medical Physics 40 (2013) 063504.
- 830 [62] W. Shao, E. Sarah, Y. Gerard, T. J. Pan, Patton, J. M. Reinhardt, O. C.,
831 J. E. B. Durumeric, G. E. Christensen, Sensitivity analysis of jacobian
832 determinant used in treatment planning for lung cancer, Proc.SPIE
833 Medical imaging 10574 (2018) 10574 – 10574 – 9.
- 834 [63] K. Du, J. E. Bayouth, K. Cao, G. E. Christensen, K. Ding, J. M. Rein-
835 hardt, Reproducibility of registration-based measures of lung tissue ex-
836 pansion., Medical Physics 39 (2012) 1595–1608.
- 837 [64] R. Achanta, A. Shaji, K. Smith, A. Lucchi, P. Fua, S. Süssstrunk, SLIC
838 superpixels compared to state-of-the-art superpixel methods, IEEE
839 Trans. Pattern Anal. Mach. Intell. (2012).
- 840 [65] T. N. Matin, N. Rahman, A. H. Nickol, M. Chen, X. Xu, N. Stewart,
841 T. Doel, V. Grau, J. M. Wild, F. V. Gleeson, Chronic obstructive pul-
842 monary disease: Lobar analysis with hyperpolarized 129 xe mr imaging,
843 Radiology 282 (2016) 857–868.
- 844 [66] E. M. Eslick, J. Kipritidis, D. Gradinscak, M. J. Stevens, D. L. Bailey,
845 B. Harris, J. T. Booth, P. J. Keall, Ct ventilation imaging derived
846 from breath hold ct exhibits good regional accuracy with galligas pet,
847 Radiotherapy and Oncology 127 (2018) 267–273.
- 848 [67] A. Szmul, T. Matin, F. V. Gleeson, J. A. Schnabel, V. Grau, B. W.
849 Papież, Xemri to ct lung image registration enhanced with personal-

850 ized 4dct-derived motion model, in: Image Analysis for Moving Organ,
851 Breast, and Thoracic Images, Springer, 2018, pp. 260–271.

852 **Appendix A Influence of the supervoxel size**

853 Here, we present detailed numerical results calculated for the influence of
854 the supervoxels size, based on which plots from Fig. 3 were prepared. The
855 provided Tables 2, 3, 4, 5 were used to create Fig. 3, where we investigate
856 the influence of the supervoxel size on the Spearman correlation between the
857 results of the proposed estimated ventilation method and XeMRI ventilation
858 images. In Tables 2, 3, 4, 5 we have shown the results calculated for the
859 different image registration methods, the deeds [44], demons [45], BLF [41]
860 and supervoxel graph cuts [46], respectively.

Table 2: The influence of the size of supervoxels on the Spearman correlation between 4DCT-based estimated ventilation maps using the deeds [44] registration method and XeMRI ventilation images.

Patient	$\sim 1k$	$\sim 2k$	$\sim 5k$	$\sim 10k$
1	0.364	0.471	0.421	0.423
2	0.686	0.685	0.678	0.677
3	0.209	0.282	0.263	0.259
Avg	0.419	0.479	0.454	0.453

Table 3: The influence of the size of supervoxels on the Spearman correlation between 4DCT-based estimated ventilation maps using the demons [45] registration method and XeMRI ventilation images.

Patient	$\sim 1k$	$\sim 2k$	$\sim 5k$	$\sim 10k$
1	0.220	0.351	0.336	0.302
2	0.639	0.661	0.660	0.651
3	0.255	0.336	0.315	0.292
Avg	0.371	0.449	0.437	0.415

Table 4: The influence of the size of supervoxels on the Spearman correlation between 4DCT-based estimated ventilation maps using BLF demons [41] registration method with sliding motion preservation and XeMRI ventilation images.

Patient	$\sim 1k$	$\sim 2k$	$\sim 5k$	$\sim 10k$
1	0.236	0.417	0.380	0.372
2	0.651	0.653	0.650	0.641
3	0.218	0.308	0.295	0.294
Avg	0.368	0.459	0.442	0.435

Table 5: The influence of the size of supervoxels on the Spearman correlation between 4DCT-based estimated ventilation maps using supervoxel-based graph cuts [46] registration method with sliding motion preservation and XeMRI ventilation images.

Patient	$\sim 1k$	$\sim 2k$	$\sim 5k$	$\sim 10k$
1	0.385	0.450	0.428	0.417
2	0.603	0.675	0.667	0.659
3	0.213	0.298	0.278	0.264
Avg	0.400	0.474	0.458	0.447

861 Appendix B Influence of the number of supervoxel layers

862 We present here detailed numerical results calculated for the influence of
863 the number of supervoxels layers on Spearman correlation between estimated
864 ventilation surrogates and XeMRI, based on which plots from Fig. 4 were
865 prepared.

Table 6: The influence of the number of layers of supervoxels on the Spearman correlation of XeMRI with deeds [44] registration method based ventilation surrogates.

Patient	1 layer	5 layers	10 layers	15 layers	25 layers
1	0.374	0.411	0.469	0.471	0.476
2	0.644	0.689	0.686	0.685	0.690
3	0.257	0.281	0.280	0.282	0.287
Avg	0.425	0.460	0.478	0.479	0.484

Table 7: The influence of the number of layers of supervoxels on the Spearman correlation of XeMRI with demons [45] registration method without sliding motion preservation based ventilation surrogates.

Patient	1 layer	5 layers	10 layers	15 layers	25 layers
1	0.200	0.326	0.354	0.351	0.369
2	0.500	0.662	0.663	0.661	0.667
3	0.315	0.338	0.335	0.336	0.332
Avg	0.338	0.442	0.450	0.449	0.459

Table 8: The influence of the number of layers of supervoxels on the Spearman correlation of XeMRI with BLF demons [41] registration method with sliding motion preservation based ventilation surrogates .

Patient	1 layer	5 layer	10 layer	15 layers	25 layers
1	0.254	0.334	0.361	0.417	0.426
2	0.562	0.638	0.653	0.653	0.656
3	0.300	0.308	0.302	0.308	0.313
Avg	0.372	0.426	0.439	0.459	0.465

Table 9: The influence of the number of layers of supervoxels on the Spearman correlation of XeMRI with supervoxel-based graph cuts [46] registration method based ventilation surrogates.

Patient	1 layer	5 layer	10 layer	15 layers	25 layers
1	0.291	0.377	0.398	0.450	0.477
2	0.652	0.677	0.671	0.675	0.678
3	0.275	0.289	0.297	0.298	0.299
Avg	0.406	0.448	0.455	0.474	0.485